Computers and Fluids 179 (2019) 27–33

Contents lists available at ScienceDirect

Computers and Fluids

journal homepage: www.elsevier.com/locate/compfluid

Development of in/outflow boundary conditions for MPM simulation of uniform and non-uniform open channel flows

Xuanyu Zhao[a,*], Marco Bolognin[b], Dongfang Liang[a], Alexander Rohe[c], Philip J. Vardon[b]

[a] Department of Engineering, University of Cambridge, Cambridge CB2 1PZ, UK
[b] Faculty of Civil Engineering and Geosciences, Delft University of Technology, Delft GA 2600, the Netherlands
[c] Deltares, Delft HV 2629, the Netherlands

ARTICLE INFO

Article history:
Received 2 May 2018
Revised 20 September 2018
Accepted 5 October 2018
Available online 6 October 2018

Keywords:
Material point method
Inflow/outflow boundary conditions
Open channel flows
Free overfall

ABSTRACT

This paper describes the development and application of inflow and outflow boundary conditions (BCs) for the material point method (MPM) in order to simulate fluid flow problems. This corresponds to velocity and pressure controlled BCs. Due to the coupled Lagrangian and Eulerian description of the fluid motion in MPM it is necessary to add and remove material points, with appropriate kinematic properties, to and from the computational domain. The newly-developed BCs have been used to simulate uniform open channel flow and the phenomenon of free overfall in open channels, which is transient conditions leading to non-uniform flow due to a sudden bed level drop. It is shown that the numerical results predict well the flow geometry including end depth ratio, pressure distribution and accelerations, therefore the velocities and displacements.

1. Introduction

Free surface fluid flows are common problems in many fields of engineering. Several arbitrary Lagrangian–Eulerian (ALE) methods have been developed for fluid dynamics in recent years (e.g. [1–4]) to simulate free surface flow. The material point method (MPM) [5] is a specific variant of an ALE method.

MPM is a well-suited method for the solution of flow-like problems involving arbitrary large deformations in continuum mechanics [4,6–10]. In particular, MPM is well suited for the coupled simulation of fluid and solids, where large deformation and history tracking of variables is required.

The position of the material is traced by the material points (MPs) thus no specific procedure is needed to capture or to trace interfaces. MPs can move through a fixed background mesh during the simulation and, consequently, in order to model continuous flows, MPs must be inserted to and/or removed from the domain at boundaries. This paper describes the development, verification and validation of velocity-controlled inflow and pressure-controlled outflow BCs for MPM. The implementation has been undertaken in the Anura3D software (www.anura3d.com).

Originally, the modelling approach to simulate quasi-steady in/outflow conditions in MPM was to use large reservoirs in order to supply the domain of interest with MPs (e.g. [11–13]). This required a large reservoir, increasing the computational effort, only approximated steady conditions and limited the time able to be simulated. Being able to prescribe in/outflow BCs allows: (i) true steady-state conditions; (ii) a large reduction of computational cost; (iii) the simplification of the geometry; and (iv) improving the general applicability of the method.

The proposed algorithm allows the enforcement of different upstream and downstream conditions. For the purpose of model validation, the paper applies the new BCs for modelling eventual steady-state subcritical flow in an uniform open channel and free overfall, comparing the results with experimental measurements and analytical solutions.

This paper is structured as follows: in Section 2 the theoretical and numerical formulation of MPM as implemented in Anura3D is briefly introduced; Section 3 discusses the development and implementation of the proposed in/outflow BCs; in Section 4 the new algorithm is verified by simulating a subcritical flow that requires proper simultaneous imposition of upstream and downstream BCs; in Section 5 the numerical results of a free overfall flow are compared with existing analytical and experimental results as validation; and the conclusions are presented in Section 6.

* Corresponding author.
E-mail address: xz328@cam.ac.uk (X. Zhao).

https://doi.org/10.1016/j.compfluid.2018.10.007
0045-7930/

2. Theoretical and numerical formulation

2.1. Governing equations

The strong form partial differential governing equations that describe the motion of fluids are conservation equations of mass (Eq. (1)) and momentum (Eq. (2)). These are more commonly known as Navier–Stokes equations in computational fluid dynamics:

$$\frac{\partial \rho}{\partial t} + \rho \bigtriangledown \cdot \mathbf{v} = 0 \tag{1}$$

$$\rho \mathbf{a} = \bigtriangledown \cdot \boldsymbol{\sigma} + \rho \mathbf{g} \tag{2}$$

where ρ is the fluid density, t is time, $\mathbf{v}$ is the velocity, $\mathbf{a}$ is the acceleration, $\boldsymbol{\sigma}$ is the Cauchy stress tensor and $\mathbf{g}$ is the body force exerted, for example, by gravity. The Cauchy stress tensor can be decomposed in $\boldsymbol{\sigma} = p + \boldsymbol{\sigma_{dev}}$ where p is the fluid pressure and the subscript $(_{dev})$ indicates the deviatoric component of the Cauchy stress tensor. The dynamic viscosity μ is introduced into the formulation by defining $\boldsymbol{\sigma_{dev}} = \mu \dot{\boldsymbol{\varepsilon}}_{\boldsymbol{dev}}$, where $\dot{\boldsymbol{\varepsilon}}_{\boldsymbol{dev}}$ is the shear strain rate.

For weakly compressible fluids, the mass density is related to the fluid pressure as:

$$\frac{\partial \rho}{\partial t} = \frac{1}{c}\frac{\partial p}{\partial t}; \quad c = \sqrt{\frac{K}{\rho}} \tag{3}$$

where c is the compression wave velocity and K is the bulk modulus of the fluid.

In MPM, the nonlinear convective term is not present (in Eq. (2)) as a result of the Lagrangian framework [14]. Instead, the positions of the MPs are updated each time step. Heat effects or any source of thermal energy is disregarded and the mechanical work is the only considered source/sink of energy.

2.2. Numerical algorithm

The Navier-Stokes equations are discretized in space and time using standard finite element method techniques. A mixed Gauss algorithm is used in which integration is at the elements' Gauss point locations for fully filled element, and at MPs for partially filled elements, e.g. at fluid surfaces. This leads to smoother stress fields and mitigates some effects of grid crossing error [6]. Explicit time integration and tetrahedral elements with linear shape functions are used here.

MPM requires a second solution domain discretization that consists of a cluster of MPs, each one with a fixed mass. It is assumed that each MP corresponds to a representative volume of the continuum body Ω, with the initial volume V_p^0, where the superscripts $(^0)$ indicates the time step, the subscript $(_p)$ indicates the MP values and it is calculated as:

$$V_p^0 = \frac{1}{n_{ep}} \int_{d\Omega_e} d\Omega \approx \frac{1}{n_{ep}} \sum_{q=1}^{n_{eq}} w_q |\mathbf{J}(\mathbf{x}_q)| \tag{4}$$

where n_{ep} is the number of points per element, n_{eq} is the number of integration points (i.e. Gauss points or MPs) per element, $d\Omega_e$ is the volume associated with the eth tetrahedral element, so that $\Omega = \bigcup_{el=1}^{n_{el}} \Omega_{el}$, w_q is the local integration weight associated with the integration point $(_q)$, $\mathbf{J}$ is the Jacobian matrix, $\mathbf{x}_q$ is the position vector.

Information can be mapped between points and nodes by linear interpolation with the same shape functions used for the mapping between global and local coordinate systems. This process is done in fully filled elements to map information to the integration points location prior to numerical integration. For example, when mapping information between nodes and MPs, a displacement field $\mathbf{u}$ can be written as:

$$\mathbf{u}_p(\mathbf{x}_p) \approx \sum_{j=1}^{n_n} N_j(\mathbf{x}_p)\mathbf{u}_j(t) \tag{5}$$

in which the subscript $(_j)$ indicates the nodal values, n_n is the number of nodes per element and N is the interpolation function (from the combination of linear shape functions of the nodes evaluated in global coordinate system). The same interpolation can be applied for other quantities (i.e. acceleration, mass, stress, etc.).

The details of the mathematical framework, including a description of the computational cycle can be found in, e.g., [15]. Using the constitutive equation (Eq. (3)) and the standard finite element method (FEM) spatial discretisations, the weak form of the momentum balance equation (Eq. (2)) can be written as:

$$\mathbf{M}_j^t \mathbf{a}_j^t = \mathbf{F}_j^{\text{int},t} + \mathbf{F}_j^{\text{ext},t} \tag{6}$$

where $\mathbf{M}$ is the lumped mass matrix, $\mathbf{F}^{\text{int}}$ and $\mathbf{F}^{\text{ext}}$ are the internal and external nodal forces and $\mathbf{a}$ is the vector of nodal acceleration. These are respectively defined as:

$$\mathbf{M}_j^t = \sum_{e=1}^{n_{ej}} \sum_{q=1}^{n_{eq}} N_j(\mathbf{x}_q) m_q \Big|_t \tag{7}$$

$$\mathbf{F}_j^{\text{int},t} = \sum_{e=1}^{n_{ej}} \sum_{q=1}^{n_{eq}} \mathbf{B}_j^T(\mathbf{x}_q)\boldsymbol{\sigma}_q V_q \Big|_t \tag{8}$$

$$\mathbf{F}_j^{\text{ext},t} = \sum_{e=1}^{n_{ej}} \sum_{q=1}^{n_{eq}} m_q N_j(\mathbf{x}_q)\mathbf{g} \Big|_t + \mathbf{f}_j^{\text{ext}} \Big|_t \tag{9}$$

where $\mathbf{B}$ is the strain-displacement matrix, $\mathbf{f}_j^{\text{ext}}$ are the prescribed boundary nodal tractions and m_q is the mass associated with the integration point in consideration. The general MPM explicit numerical algorithm for weakly compressible Navier Stokes solution is as follows:

1. Map the information carried by the MPs to the background mesh using linear shape functions;
2. Determine the lumped mass matrix (Eq. (7)), the internal force $\mathbf{F}^{\text{int}}$ (Eq. (8)) and external force $\mathbf{F}^{\text{ext}}$ (Eq. (9)) vectors at the nodes;
3. Compute the nodal acceleration field from (Eq. (6)), imposing zero acceleration at the inflow nodes (see Fig. 1a);
4. MP velocities are updated using the nodal acceleration as:

$$\mathbf{v}_p^{t+1} = \mathbf{v}_p^t + \Delta t \sum_{j=1}^{n_n} N_j(\mathbf{x}_p)\mathbf{a}_j^t \tag{10}$$

5. The MP positions are updated:

$$\mathbf{x}_p^{t+1} = \mathbf{x}_p^t + \Delta t \sum_{j=1}^{n_n} N_j(\mathbf{x}_p)\mathbf{v}_j^{t+1} \tag{11}$$

6. The incremental MP strains are calculated as:

$$\Delta\varepsilon_p^{t+1} = \mathbf{B}(\mathbf{x}_p)\Delta\mathbf{u}_j^{t+1} \tag{12}$$

7. The stresses are derived from the constitutive relation (Eq. (3));
8. Determine the density of MPs, which is used to update the MP's volumes, as:

$$\rho_p^{t+1} = \frac{\rho_p^t}{1 + \Delta\varepsilon_{\text{vol},p}^{t+1}} \tag{13}$$

where $\varepsilon_{\text{vol},p}^{t+1}$ is the incremental volumetric strain.

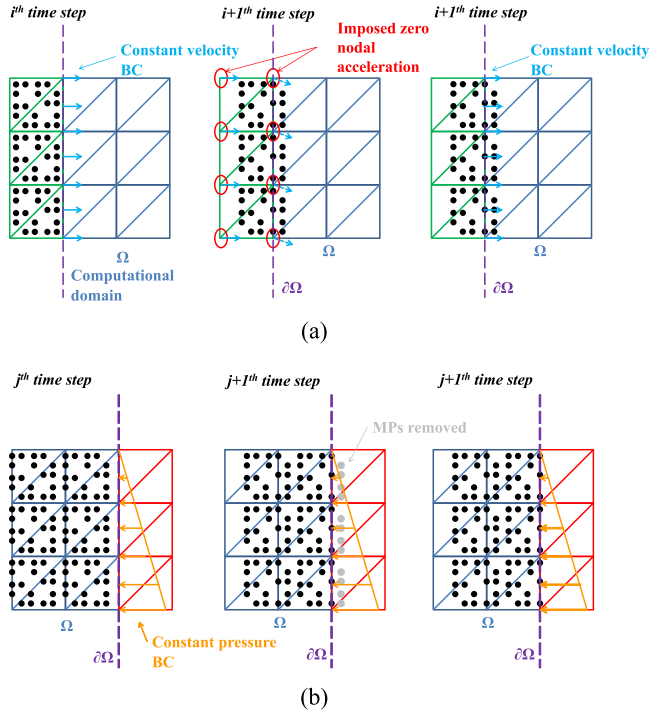

Fig. 1. Illustration of the BCs: (a) Inflow BC, with inflow elements (green) and (b) outflow BC, with outflow elements (red). (For interpretation of the references to colour in this figure legend, the reader is referred to the web version of this article.)

In order to solve the system of governing equations, it is possible to distinguish three kinds of BCs: essential (Dirichlet, acceleration), natural (Neumann, force) or a combination of the two (e.g. Newton/Robin). Other state variables, i.e. acceleration, velocitiy and pressure in this case, also need to be initialised. Further, strain and pressure smoothing procedures are used to mitigate the stress oscillations due to grid crossing [16].

To ensure the stability of the explicit scheme, the critical time step should satisfy the so-called *Courant–Friedrichs–Levy (CFL)* condition [17], meaning that the time increment should not exceed a certain value depending on material density, stiffness and the minimum size of the elements.

$$\Delta t_{\text{crit}} = \frac{l_e}{c_p} \tag{14}$$

where Δt is the critical time step, l_e is the minimum length of the element. In our study, a reduction factor α_{Courant} is introduced in the above expression to obtain the time step size (i.e. $\Delta t = \alpha_{\text{Courant}} \times \Delta t_{\text{crit}}$), where α_{Courant} is fixed as 0.98 in our study.

3. In/outflow boundary conditions

Fluid flows are problems of practical interest for many engineering applications. Their simulation requires accurate and efficient numerical methods in versatile numerical tools that can be further used to study real industrial problems [18]. As opposed to solid mechanics problems, in problems which consider fluid flowing, mass generally enters and leaves an area of interest. For example, this may be the flow over a weir or dyke overtopping where the area of interest is fixed around the structure (the weir or dyke) and water flows into and out of the area. This may also apply in, for example, porous media or in erosional or depositional processes. Therefore, to make an efficient computational solution, BCs allowing this mass to enter or leave the domain under realistic conditions are essential. The novel contribution here is the description of well-posed problems able to simulate flows, with special emphasis on BCs.

BCs exist in nature as natural boundaries. Due mainly to limitations in computational power, large domains are often truncated and confined between artificial boundaries (ABCs). The location of the required ABCs can be fabricated by intuition, experience, asymptotic behaviour and numerical experimentation [19]. Clearly, the minimal necessary requirement of ABCs is to ensure the solvability of the truncated problem, but this does not ensure a physcially reasonable response.

To simulate a segment of a flow, the BCs must allow mass to enter and leave the domain at a predefined flowrate, and to control the pressure imposed from the water outside the boundary. For a solvable governing equation, all boundaries must only have one of these ABCs. However, this would not necessarily (i) impose a prescribed flow, or (ii) ensure mass enters and leaves the domain between timesteps. To ensure a segment of flow is achieved, a specific combination of ABCs to solve the governing equation along with a strategy on how to consistently add and remove mass (to ensure mass continuity and thus satisfying Eq. (1) is needed. These are here termed inflow and outflow BCs.

One of the BCs must control the kinematics, i.e. fix the acceleration or velocity. If both the inflow and outflow conditions control kinematics, physically impossible situations may arise, e.g. not enough mass in the domain to satisfy the ABC, this could be considered to be over-defined. If neither BCs controls the kinematics, the problem is not well-posed. Many flow segments finish in either subcritical hydraulic conditions or zero pressure conoditions and therefore a pressure boundary is more appropriate for the outflow boundary. Therefore, the inflow boundary has been selected to control the kinematics.

A steady inflow is considered here for the inflow boundaries, although it would be straightforward to update this procedure for a temporally varying inflow. A fixed pressure is considered for the outflow boundaries; again it would be straightforward to update this procedure to change in time. To consistently add and remove mass, an ad-hoc element layer is attached to the computational domain where the ABCs are applied.

The steady inflow BC, i.e. constant velocity and zero acceleration, is applied to the boundary shown by the dotted line in Fig. 1a. The ad-hoc element layer, called here inflow elements (shown in green in Fig. 1a), is added to the computational domain (shown in blue). At the beginning of the computational cycle, MPs are placed in the inflow elements with appropriate Initial Conditions (ICs), i.e. the prescribed velocity and zero acceleration. The inflow nodes that are shared with the elements of the computational domain (highlighted in Fig. 1a by red ellipses) have a prescribed acceleration (zero) so as to maintain the prescribed velocity field at the boundary, applied to the solution of the governing equation by updating **a** in step 3 of Section 2.2. When an inflow element is empty, new MPs will be introduced in the inflow elements at the same local position as material which is initially discretized inside the domain, i.e. the Gauss point locations. Since the mass of the MPs is initialized according to the initial (inflow) element volume and it is constant throughout the calculation, it is straightforward to impose a velocity such that the MPs move by the length of one element before a new set of MPs can be introduced, i.e. at every n^{th} time step, defined as:

$$n = \frac{\Delta L}{\mathbf{v}^0 \Delta t_i} \tag{15}$$

where ΔL is the element size in direction parallel to the prescribed velocity vector, $\mathbf{v}^0$ is the prescribed input velocity and Δt_i is the i^{th} time step size.

In order to impose on the outflow BC, a fixed pressure is required at the boundary. This is achieved by fixing the external

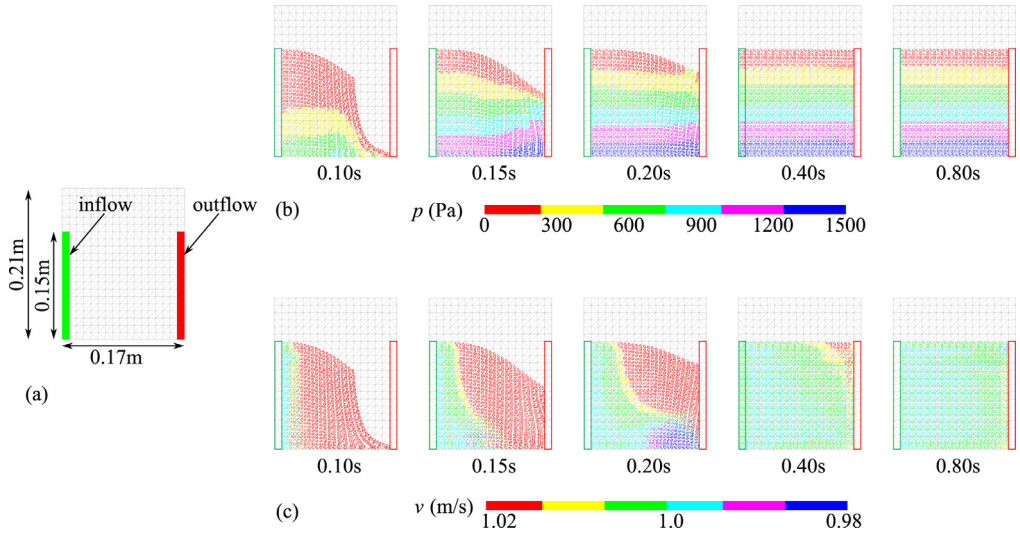

Fig. 2. (a) Computational mesh of a rectangular channel and application of in/outflow BCs for the simulation of a subcritical flow. Representation of the fluid flow converging to a steady solution enforced by the downstream BC: (b) Pressure field; (c) Velocity field at different time steps.

forces at the nodes of the background grid at the boundary. Again a strategy of removing mass is needed: MPs are removed from the computational domain as soon as they enter an outflow element. If one desires to model the outflow of a steadily flowing fluid, it is reasonable to assume a hydrostatic distribution of the pressure on the outflow nodes when solving the momentum balance equations, although any pressure distribution could be applied.

For the outflow BC, additional elements, called outflow elements, are also introduced (Fig. 1b). The fixed pressure BCs are assigned on the nodes shared with the computational domain in step 2 of Section 2.2. As soon as a MP enters an outflow element it is removed from the computation. The target level of accuracy of the numerical solver can be systematically achieved adjusting time and space discretization.

4. Verification of boundary conditions

In order to verify the application of the in/outflow BCs a simple case is simulated. An initially empty domain is considered of $0.15 \times 0.15 \times 0.01$ m, in x-, y-, z-direction, with frictionless walls, a prescribed horizontal inflow velocity of 1.0 m/s and a zero acceleration along the inflow boundary as indicated in Fig. 2a. The three-dimensional domain is discretised by linear tetrahedral elements and has a thickness of one element with only the front face shown in Fig. 2. A band of outflow elements is attached to the right side of the computational mesh with a prescribed hydrostatic pressure. Outflow elements and their BCs are only activated when MPs enter the adjacent elements. The water is modelled by a Newtonian compressible constitutive model. It has an initial density $\rho^0 = 1000\,\text{kg/m}^3$, dynamic viscosity $\mu = 1 \times 10^{-6}$ kPa · s and bulk modulus $K = 20{,}000$ kPa. The water bulk modulus was reduced by a factor of 100 from reality in order to increase the time step as an explicit integration scheme is adopted. It was pointed out in Liang [20] that, as long as the modelled water has a speed of sound over 10 times larger than the maximum flow velocity, the increased compressibility of water does not significantly affect the results. The minimum time step is obtained as described in Section 2.2.

Fig. 2 shows the simulation results in terms of pressure (b) and velocity (c) at different time steps. After an initial time interval of transient moving water front, a steady uniform flow is achieved. It is worth mentioning that the prescribed traction BC at the outflow boundary nodes causes unreasonably high pressures near the bottom when the flow is not yet fully developed, which is especially evident at 0.15 s and 0.20 s. This is caused by the prescribed hydrostatic pressure which is initiated based on the final water depth. As the calculation continues, and the outlet water level keeps rising, this inconsistency vanishes. This phenomenon can be avoided if the hydrostatic pressure at the outflow elements would be updated during calculation based on the water depth. However, the purpose of present simulation is to verify the capabilities of the newly proposed in/outflow BCs. After 0.8 s it can be seen that a constant velocity, a hydrostatic pressure and a horizontal free surface is achieved, which proves the correctness of the applied BCs.

5. Validation benchmark

In order to validate the theoretical formulation and numerical implementation of in/outflow BCs, a well-known open channel flow problem has been simulated. This is the situation where a fluid flow encounters a sudden drop at the bed, also known as a free overfall. The free overfall simulation is chosen as validation benchmark for the in/outflow BCs since the rapid change in bed geometry is considered a stringent validation case.

5.1. Existing free overfall studies

Rouse [21] measured the pressure distribution in a steady horizontal rectangular free overfall using wall and bed piezometers. It was observed that a free overfall in rectangular channels could be used as a simple flow measuring device that required no calibration. Since then, due to its practical importance, many investigators have studied free overfall in various channels (e.g., [22–24]). In [24], water was provided from a constant head tank supplied by a pump and was measured by means of a calibrated orifice meter located in the supply line. At the end of the channel, the side walls were continued beyond the brink so that the nappe was confined between the side walls. The water surface profile was measured by means of a point gauge. The pressure distribution at the end section, as well as in the upstream region, was measured.

When the free overfall enters the air, there is no reverse curve in the water surface until it strikes the bottom at a lower elevation. According to the momentum conservation law, provided that no external energy is added to the system, the water surface will seek its lowest possible energy configuration. The theoretical flow depth for parallel flows with a rectangular cross-section is then

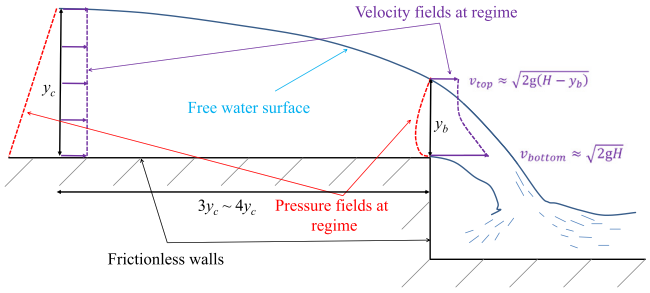

Fig. 3. Free overfall problem.

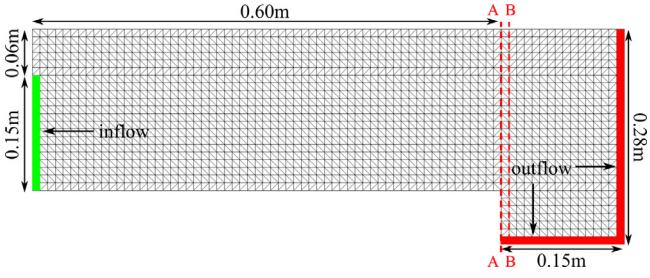

Fig. 4. Computational mesh of a rectangular channel for free overfall simulation. The in/outflow BC elements are highlighted respectively in green and red. At the overfall brink two cross sections (A-A and B-B) are investigated. (For interpretation of the references to colour in this figure legend, the reader is referred to the web version of this article.)

equal to the critical flow depth y_c, as shown in Fig. 3 [25], where H is the total water head. The critical flow depth y_c is expressed as $y_c = \sqrt[3]{\alpha(\bar{v}h_i)^2/g}$, where $\bar{v}$ is the mean flow velocity of the cross-section, h_i is the initial flow depth and α is the velocity coefficient which can be approximately taken as 1.0 .

For the free overfall flow and rapidly varied bed geometry problems, the actual surface follows the profile represented by the solid blue line in Fig. 3. Rouse [21] experimentally found that for almost horizontal geometries, the computed critical depth based on parallel flow assumption y_c is about 1.4 times the brink depth y_b.

Montes [26] proposed an analytical solution for the analysis of open channel flows near a discontinuity of the bed geometry (i.e. free overfall). Assuming the flow in each terminal section to be nearly parallel with the bottom, negligible viscous effects, irrotational flow and energy conservation, it is possible to use a potential-flow solution of the inverse type (a variant of Stokes inverse mapping [27]). The solution of the potential-flow equations was solved numerically by a finite difference grid (successive over relaxation method), and the unknowns (free-surface location, velocity and pressure fields) were determined by an iterative procedure. This solution is used as reference for the numerical solution as shown in Figs. 7 and 8.

Readers are referred to Dey [28] for a comprehensive review of the research on free overfall in rectangular open channels flows.

5.2. Computational setup

In Fig. 4, an initially empty section of the computational domain of $0.60 \times 0.21 \times 0.01$ m in x-, y-, z-direction represents a rectangular open channel with a sudden discontinuity of the bed on the bottom right part represented by an additional section of the computational domain of $0.15 \times 0.28 \times 0.01$ m in x-, y-, z-direction. A 0.15 m deep inflow BC with horizontal velocity of 1.213 m/s is prescribed as indicated in green in Fig. 4. All contact surfaces of the domain are frictionless. As in the subcritical flow case (Section 4), the three-dimensional domain is discretised by linear tetrahedral elements and has a thickness of one element with only the front face shown in Fig. 4. An outflow BC is prescribed to the right and bottom right boundaries of the computational mesh (outflow elements shown in red), with zero traction prescribed at the nodes. The cross section for the analysis of the result around the brink are shown in Fig. 4. Frictional effects are neglected for all contact surfaces. The material properties (e.g. density, viscosity and bulk modulus) are as assigned in Section 4 and the time step is calculated as in Section 2.2. In the following section, the dependencies of the simulation results on the number of material points per element and mesh size are evaluated.

5.3. Results

5.3.1. Effect of mesh size and number of material points per element

A sensitivity study of the free overfall simulations by varying the computational mesh size and the initial number of material points per element (PPE) is given in this section. Figs. 5 and 6 show results of open channel flow simulations with initial water depth of 0.15 m and velocity of 1.213 m/s. Three mesh sizes are used: 0.03 m, 0.01 m and 0.005 m when studying the effect of the mesh size, and 4 PPEs are used as first approximation (Fig. 5).

It can be observed that there are frequent pressure fluctuations when using finer meshes which are attributed to grid-crossing errors. It is discussed in Guilkey et al. [29] and Al-Kafaji [6] that using a finer mesh causes more frequently migration of MPs between elements and therefore, the grid-crossing errors are more

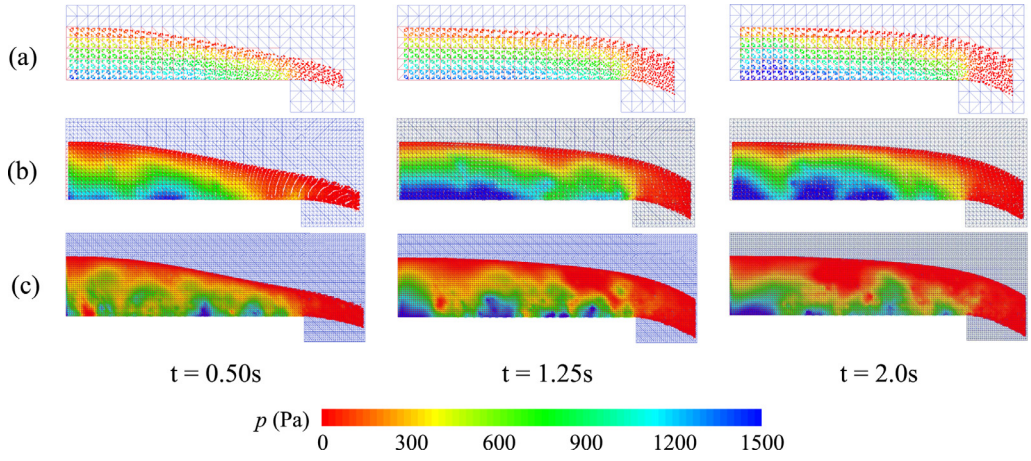

Fig. 5. Comparison of open channel simulations with different mesh sizes. a) $\Delta L = 0.03$ m; b) $\Delta L = 0.01$ m; c) $\Delta L = 0.005$ m for different time instants.

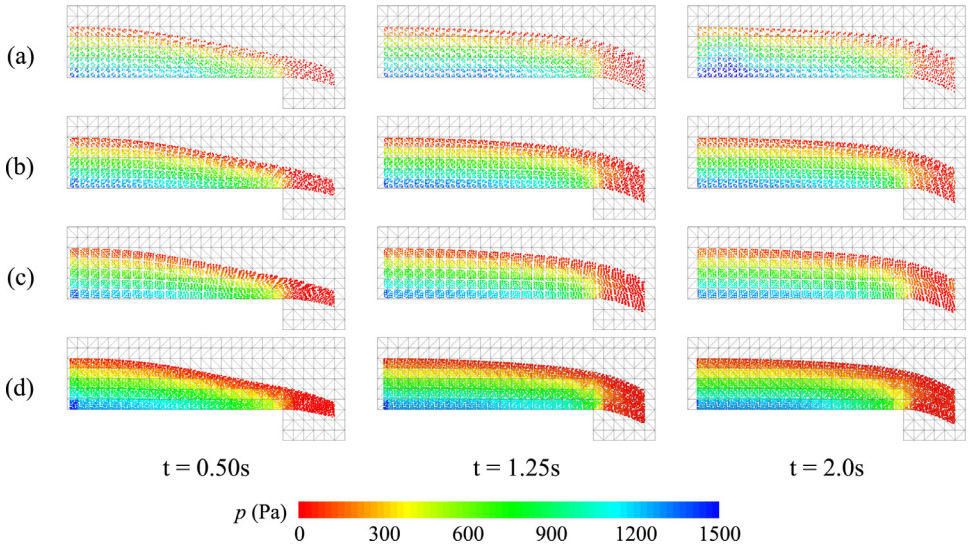

Fig. 6. Comparison of open channel simulations with different PPEs. a) PPE = 4; b) PPE = 8; c) PPE = 10; d) PPE = 20 for different time instants.

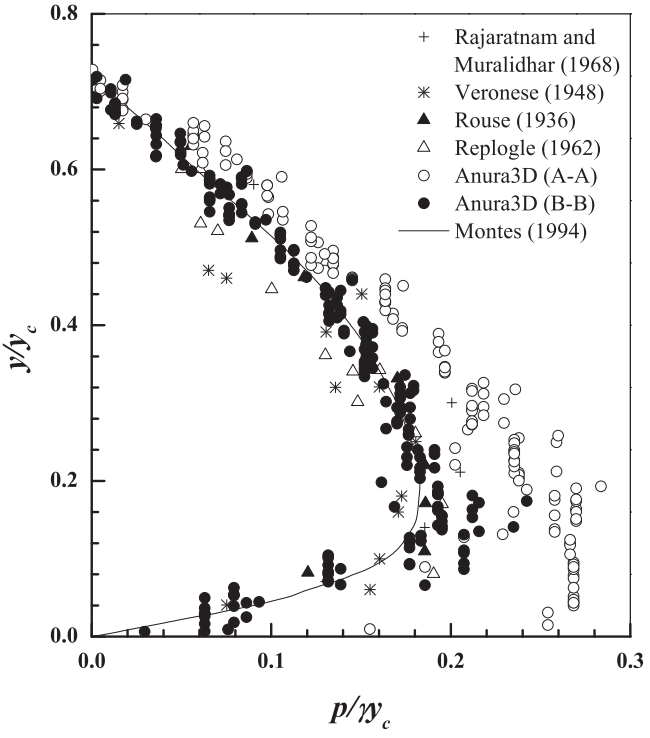

Fig. 7. Pressure distribution at brink in rectangular overfall.

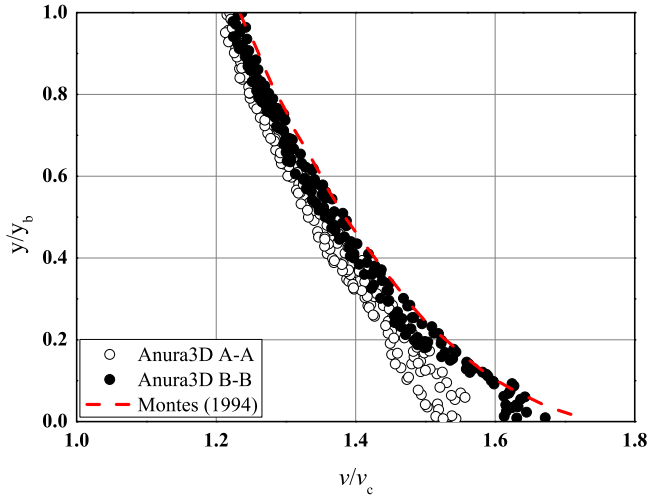

Fig. 8. Fluid velocity at the brink. Comparison of analytical solution with MP velocity for steady state flow conditions.

Table 1
Relative error of brink depth estimation using meshes with various sizes (8 PPE) .

Mesh size (m)	Time (s)	y_b (s)	Analytical (m)	Error (%)
0.03	2	0.1109	0.10725	3.44
0.01	2	0.1093	0.10725	1.90
0.005	2	0.1093	0.10725	1.88

pronounced. The problem is more severe when the PPE is low [6] and the stiffness of the material is high. However, the mesh resolution plays an important role for the accuracy of the results: decreasing the mesh size the brink height in the numerical solution converges to the analytical one (see Table 1, where 8 PPE are used).

Fig. 6 shows the comparison of simulations of open channel flow with four different values of PPE: 4, 8, 10 and 20 MPs per element, respectively for a mesh size of 0.03 m. It can be observed that 4 PPE is a too coarse discretisation as it emphasises the grid crossing error while simulations with 8, 10 and 20 PPE produce much better results in terms of pressure distribution.

These results led to the conclusion that the nodal density oscillations are the main cause of pressure fluctuations due to the weakly compressible behaviour of the fluid. The change in calculated nodal density in this method is directly due to the proportional change in PPE in the elements surrounding the node, and therefore by increasing the PPE the oscillations are reduced. Table 1 gives a quantitative analysis of the brink depth relative error combining different mesh sizes and using 8 PPE. In this paper, we propose to use a finer mesh because that improves the depth at the brink and the drawback of more pressure oscillation is compensated by introducing a higher number of PPE.

5.3.2. Pressure distribution at brink

The pressure distribution with the numerical solution provided by MPM are compared with laboratory measurements (Section 5.1) and the analytical solution. The pressure distribution at the brink (cross-section A-A in Fig. 4) is plotted with data from literature in Fig. 7, where γ is the water unit weight and y is the height of the MP above the brink. Note that the MPs selected for analysis are actually located within a thin area (about one fifth of the element size) in the flow direction containing the chosen cross-sections. From the comparison, it can be seen that near the free surface, the numerical pressure distribution in both cross sections agree relatively well with experimental data obtained by other researchers. For the region near the bed, the numerical simulations seem to over-predict the pressure in cross section A-A. This may be attributed to the vertical fixities applied on the corner nodes of the brink, which prevent the material points from leaving the mesh. This vertical fixity also restricts the material point from moving freely downward once they pass the brink, within one element, causing the pressure near the bottom to increase. This can be shown by selecting MPs one element away (cross-section B-B in Fig. 4), where the influence of the vertical fixity is negligible, and the pressure distribution near the bed is significantly closer to the experimental results.

5.3.3. Velocity distribution at brink

Fig. 8 shows the comparison of the velocity distribution with the results calculated by semi-analytical solution given in [26], where v and v_c are the velocity and critical velocity, respectively. Material points are chosen in the same manner as in Fig. 7. It can be seen that the velocity close to the channel bed is slightly underestimated in cross-section A-A. Several factors may contribute to that: in experiments there is a slight contraction of the flow at the brink where the water detaches from the bed which is not occurring in the numerical simulation; the low order shape functions produce a slightly over stiff behaviour that reduces the velocity where the largest deformations occur. Last but not least, the impact of the fixity mentioned above also adds to underestimation of the velocity in cross-section A-A.

6. Conclusions

In/outflow BCs suitable for MPM simulations of open channel flow have been developed. These have been applied to the simulation of eventually steady subcritical flow and free overfalls in rectangular open channels to effectively validate the BCs. The brink depth, pressure distribution and velocities have been analysed for several geometries and flow velocities and a good agreement between the MPM results, analytical solutions and experimental results is seen. The BCs are considered validated and can be used to simulate a wide range of flow conditions.

Acknowledgments

Xuanyu Zhao acknowledges the support from the Fundamental Research Funds for the Central Universities, Ministry of Education of China (2017B12214). Marco Bolognin is grateful for the financial support by the NWO Project MPM-FLOW: Understanding flowslides in flood defences (Grant No. 13889). The authors are thankful for the technical support from the MPM research group at Deltares, The Netherlands. The Anura3D software is made available by the Anura3D MPM Research Community.

References

[1] Yan J, Deng X, Korobenko A, Bazilevs Y. Free-surface flow modeling and simulation of horizontal-axis tidal-stream turbines. Comput Fluids 2017;158:157–66.
[2] Cremonesi M, Ferri F, Perego U. A basal slip model for lagrangian finite element simulations of 3D landslides. Int J Numer Anal Methods Geomech 2017;41(1):30–53. doi:10.1002/nag.2544.
[3] Maljaars J, Labeur RJ, Möller M, Uijttewaal W. A numerical wave tank using a hybrid particle-mesh approach. Procedia Eng 2017;175:21–8. doi:10.1016/J.PROENG.2017.01.007.
[4] Zhang F, Zhang X, Sze KY, Lian Y, Liu Y. Incompressible material point method for free surface flow. J Comput Phys 2017;330:92–110. doi:10.1016/j.jcp.2016.10.064.
[5] Sulsky D, Chen Z, Schreyer H. A particle method for history-dependent materials. Comput Methods Appl Mech Eng 1994;118(1–2):179–96.
[6] Al-Kafaji IKJ. Formulation of a dynamic material point method (MPM) for geomechanical problems. Stuttgart University, Germany; 2013.
[7] Bandara SS. Material point method to simulate large deformation problems in fluid-saturated granular medium. University of Cambridge, UK; 2013.
[8] Soga K, Alonso E, Yerro A, Kumar K, Bandara S. Trends in large-deformation analysis of landslide mass movements with particular emphasis on the material point method. Géotechnique 2016;66(3):248–73. doi:10.1680/jgeot.15.LM.005.
[9] Wang B, Vardon PJ, Hicks MA. Investigation of retrogressive and progressive slope failure mechanisms using the material point method. Comput Geotech 2016;78:88–98. doi:10.1016/j.compgeo.2016.04.016.
[10] Li J, Hamamoto Y, Liu Y, Zhang X. Sloshing impact simulation with material point method and its experimental validations. Comput Fluids 2014;103:86–99.
[11] Zhao X, Liang D. MPM modelling of seepage flow through embankments. In: Proceedings of the twenty-sixth (2016) international ocean and polar engineering conference; 2016. p. 1161–5. ISBN 9781880653883. Rodos, Greece doi:10.13140/RG.2.2.33519.23208.
[12] Bolognin M, Martinelli M, Bakker KJ, Jonkman SN. Validation of material point method for soil fluidisation analysis. J Hydrodyn 2017;29(3):431–7. doi:10.1016/S1001-6058(16)60753-9.
[13] Martinelli M, Tehrani FS, Galavi V. Analysis of crater development around damaged pipelines using the material point method. Procedia Eng 2017;175:204–11. doi:10.1016/J.PROENG.2017.01.010.
[14] Sulsky D, Zhou S-J, Schreyer HL. Application of a particle-in-cell method to solid mechanics. Comput Phys Commun 1995;87:236–52.
[15] Ceccato F, Yerro A, Chmelnizkij A, Fern EJ, Martinelli M, Rohe A. Scientific manual MPM software Anura3D. Tech. Rep.. Delft: Deltares; 2017. www.anura3d.com.
[16] Martinelli M. Soil-water interaction with material point method. Tech. Rep.. Delft, the Netherlands: Deltares; 2016.
[17] Courant R, Friedrichs K, Lewy H. On the partial difference equations of mathematical physics. IBM J Res Dev 1967;11(2):215–34. doi:10.1147/rd.112.0215.
[18] Constant E, Favier J, Meldi M, Meliga P, Serre E. An immersed boundary method in openfoam : verification and validation. Comput Fluids 2017;157:55–72.
[19] Papanastasiou TC, Malamataris N, Ellwood K. A new outflow boundary condition. Int J Numer Methods Fluids 1992;14(5):587–608. doi:10.1002/fld.1650140506.
[20] Liang D. Evaluating shallow water assumptions in dam-break flows. Proc ICE Water Manage 2010;163(5):227–37.
[21] Rouse H. Discharge characteristics of the free overfall: use of crest section as a control provides easy means of measuring discharge. Civil Eng ASCE 1936;6(4):257–60.
[22] Veronese A. Rilievi sperimentali sugli sbocchi liberi. L'Energia Elettrica 1948:441–638.
[23] Replogle J. Discussion on 'end depth at a drop in trapezoidal channels' by M.H. diskin. J Hydraul Div 1962;88(2):161–5.
[24] Rajaratnam N, Muralidhar D. Characteristics of the rectangular free overfall. J Hydraul Res 1968;6(3):233–58. doi:10.1080/00221686809500236.
[25] Chow VT. Open-channel hydraulics. New York: McGraw-Hill; 1959.
[26] Montes JS. Potential flow solution to 2D transition from mild to steep slope. J Hydraul Eng 1994;120(5):601–21. doi:10.1061/(ASCE)0733-9429(1994)120:5(601).
[27] Stokes G.G.. Supplement to a paper on the theory of oscillatory waves. In: Mathematical and Physical Papers vol.1. Cambridge: Cambridge University Press; p. 314–326. doi:10.1017/CBO9780511702242.016.
[28] Dey S. Free overall in open channels: state-of-the-art review. Flow Meas Instrum 2002;13(5–6):247–64. doi:10.1016/S0955-5986(02)00055-9.
[29] Guilkey JE, Hoying JB, Weiss JA. Computational modeling of multicellular constructs with the material point method. J Biomech 2006;39(11):2074–86. doi:10.1016/j.jbiomech.2005.06.017.